

DRAFT VERSION JANUARY 8, 2022

Typeset using L^AT_EX preprint style in AASTeX62

Followup ground-based observations of the dwarf nova KZ Gem

ZHIBIN DAI (戴智斌),^{1, 2, 3, 4, 5} PAULA SZKODY,⁶ JOHN R. THORSTENSEN,⁷ AND
N. INDIKA MEDAGANGODA⁸

¹*Yunnan Observatories, Chinese Academy of Sciences, 396 Yangfangwang, Guandu District, Kunming, 650216, China.*

²*Key Laboratory for the Structure and Evolution of Celestial Objects, Chinese Academy of Sciences, 396 Yangfangwang, Guandu District, Kunming, 650216, China.*

³*Center for Astronomical Mega-Science, Chinese Academy of Sciences, 20A Datun Road, Chaoyang District, Beijing, 100012, China.*

⁴*University of Chinese Academy of Sciences, No.19(A) Yuquan Road, Shijingshan District, Beijing, 100049, China*

⁵*Key Laboratory of Optical Astronomy, National Astronomical Observatories, Chinese Academy of Sciences, Beijing 100101, China*

⁶*Department of Astronomy, University of Washington, Seattle, WA, 98195, USA.*

⁷*Department of Physics and Astronomy, Dartmouth College, 6127 Wilder Laboratory Hanover, NH 03755, USA.*

⁸*Astronomy Division, Arthur C. Clarke Institute for Modern Technologies, Sri Lanka.*

ABSTRACT

We present spectroscopy of stars in the immediate vicinity of the dwarf nova (DN) KZ Gem to confirm its identification, which had been ambiguous in the literature. Analysis of 73 radial velocities spanning from 2014 to 2019 provides a high-precision orbital period of 0.2224628(2) d (~ 5.34 hr) and shows KZ Gem to be a double-lined DN. Time series photometry taken from 2016 to 2018 shows a variable double-hump modulation with a full amplitude of ~ 0.3 mag, along with five Gaussian-like transient events lasting ~ 30 min or more. Using the light curve code XRBinary and nonlinear fitting code NMfit, we obtain an optimized binary model of the dwarf nova (DN) KZ Gem, from time series photometry, consisting of a Roche-lobe-filling K type dwarf with a mass transfer rate of $2.7 - 7.9 \times 10^{-10} M_{\odot} \text{ yr}^{-1}$ to a large, cool and thick disk surrounding a white dwarf, in an orbit with an inclination of $51^{\circ}.6(\pm 1^{\circ}.4)$. Two hotspots on the disk are demonstrated to cause the observed variations in the ellipsoidal modulations from the secondary star. This physical model is compatible with the Gaia distance of KZ Gem.

Keywords: Stars : binaries : close; Stars : cataclysmic variables; Stars : individual(KZ Gem)

1. INTRODUCTION

Hoffmeister (1966) and Kukarkin et al. (1968) first discovered KZ Gem as a variable star a half century ago. It is listed in various catalogs of cataclysmic variables (CVs; Downes & Shara e.g.

1993; Downes et al. e.g. 1997, 2001; Ritter & Kolb e.g. 2003) as a dwarf nova (DN). Since KZ Gem falls within the field of view of the K2 Campaign 0 (K2-C0), it was proposed as a CV target and observed in long cadence (30 min sampling) mode. In the K2 variable catalog¹, KZ Gem was listed as OTHPER (i.e., other periodic and quasi-periodic variables (Armstrong et al. 2015, 2016)). The “self-flat-fielding” (SFF) corrected light curve of KZ Gem (Vanderburg & Johnson 2014; Vanderburg 2014) shows an ellipsoidal-like effect. Dai et al. (2017) applied a phase-correction method to these data to show that the orbital period is 0.22242 d, almost exactly twice the orbital period of 0.11122 d listed in RKcat (Edition 7.24; Ritter & Kolb 2003). A DN outburst of KZ Gem was detected in 2015 January by Lange (2016), but without a published spectrum, KZ Gem remained a poorly understood DN.

The coordinates for KZ Gem given in RKcat and the VSX (Variable Star Index) databases of the AAVSO² differ by 9'' from those in SDSS, SIMBAD, and K2. Because the field of KZ Gem is crowded, a difference of 9'' is large enough to cause an incorrect identification. Fig. 1 shows 6 stars within 15'' of KZ Gem; Table 1 lists the SDSS coordinates of these stars. The two different coordinates listed for KZ Gem correspond to stars S1 and S3, which are marked by blue rectangles in Fig. 1. The crowding in the field also leaves open the possibility that the ellipsoidal modulation found by Dai et al. (2017) in the K2 light curve might arise from a neighboring star rather than KZ Gem.

This paper presents ground-based spectroscopy of four of the nearby stars (S1, S2, S3, and S4) and photometry of S3. In Section 2, we confirm that the identification of S3 with KZ Gem, and in Section 3 we obtain a high-precision orbital period from radial velocities. Folding with this period, the light-curve morphology, models and five transient events are discussed.

2. OBSERVATIONS

Table 2 gives a journal of the observations.

2.1. Spectroscopy

Our spectra are from four different instruments on three different telescopes. (1) With the Double Imaging Spectrograph (DIS) on the Apache Point Observatory (APO) 3.5m telescope, we obtained spectra on 5 nights using the blue and red channels simultaneously. Gratings B1200/R1200 gave a dispersion of $\sim 0.6 \text{ \AA pixel}^{-1}$. (2) With the Beijing Faint Object Spectrograph (BFOSC) and grating G4, on the Xinglong Observatory (XLO) 2.16m telescope, we obtained spectra on 3 nights with a resolution of ~ 2000 ($2.97 \text{ \AA pixel}^{-1}$). (3) With the modspec on the Hiltner 2.4m telescope at Michigan-Dartmouth-MIT (MDM) Observatory in Kitt Peak, Arizona, we obtained spectra on 12 nights spread over four observing runs (2014 December, 2016 January, 2016 February, and 2018 November). A 600 line mm^{-1} grating gave $\sim 3.5 \text{ \AA}$ resolution from 4310 to 7500 \AA , with vignetting toward the ends of the range. (4) Also with the 2.4m MDM telescope, we used the Ohio State Multi-Object Spectrograph (OSMOS) on 6 more nights in 2018 December and 2019 January, with the aim of disambiguating the long-term velocity cycle count. The spectra covered from 3970 to 6870 \AA with a resolution of 3 \AA FWHM. Flux standards were observed when appropriate, and comparison lamps were observed to maintain accurate wavelength calibration. All spectra were reduced using IRAF³.

¹ <http://archive.stsci.edu/k2/hlsp/k2varcat/search.php>

² <https://www.aavso.org/vsx/index.php?view=detail.top&oid=14553>

³ IRAF is distributed by the National Optical Astronomy Observatory, which is operated by the Association of Universities for Research in Astronomy (AURA) under cooperative agreement with the National Science Foundation.

As we show below, the spectrum of the star we identify with KZ Gem shows a contribution from a late-type secondary star. We measured absorption velocities in the MDM spectra by cross-correlating the spectra against a composite template spectrum, which was originally composed by taking 76 spectra of late-type velocity standard stars, shifting them to zero velocity, and averaging. The cross-correlation was either from the *rvsao* package (Kurtz & Mink 1998), which implements the algorithm developed by Tonry & Davis (1979), or the *fxcor* task in the IRAF *rv* package.

To estimate the secondary star’s spectral type and contribution, we shifted the individual MDM 2.4m exposures to the secondary’s rest frame and averaged the shifted spectra. We have a collection of archival spectra of K- and M-type main sequence stars classified by Boeshaar (1976) and Keenan & McNeil (1989), taken with the same instrument setup as our KZ Gem spectra, and also shifted to zero radial velocity. We estimated the secondary’s spectral type and its fractional contribution by scaling the main sequence spectra and subtracting them from the KZ Gem spectrum, interactively trying different spectral types and scaling factors until the secondary-star absorption lines were cancelled as well as possible.

2.2. Identification of KZ Gem

Inspection of Fig. 1 indicates that spectra of stars S1, S2 and S4 can be taken at the same time by using a wide slit along the north-south direction. This was accomplished on 2017 January 22. Since S1 is faint, all spectra of S1 were smoothed by a running boxcar of 5 and 3 pixels for the APO and XLO spectra, respectively. Despite the low S/N, both APO and XLO spectra of S1 (shown in the three panels of Fig. 2 and the panel a of Fig. 3) illustrate similar features of a sloping linear continuum from the blue to the red with shallow and marginal $H\alpha$ and $H\beta$ absorption lines and a lack of emission lines. Note that the $H\beta$ absorption line shown in the blue APO spectrum taken on 2016 December 05 is undetected in the following two APO spectra and the XLO spectrum. The spectra of S1 are atypical for a quiescent DN. The simultaneous spectra of the other two targets, S2 and S4 (shown in the two panels b and c of Fig. 3, respectively), also only show absorption rather than emission lines; S2 appears to be an early M-type star, and S4 is consistent with a G-type star. There is, therefore, no indication that S1, S2, and S4 are dwarf novae.

In contrast, the two XLO spectra of S3 taken on January 09 and 10, 2018 (Fig. 4) clearly show broad $H\alpha$ emission superimposed on the continuum, along with a higher blue flux level. He I emission lines are marginally visible at $\lambda\lambda$ 5876, 6678, and 7065. These features imply that S3 is the DN, confirming the coordinates listed in RKCcat, VSX and Gaia⁴. In both spectra, the He I λ 5876 emission line is blended with weak NaD absorption (as it is in DN SDSS J063213.1+253623, or J0632+2536; Dai et al. 2016), and the He I λ 5876 emission observed on 2018 January 09 appears doubled. The averaged blue and red high-resolution APO spectra are shown in Fig. 5. $H\alpha$, $H\beta$ and $H\gamma$ are visible in emission in the spectra taken on 2018 January 17 and the lower two panels of Fig. 5 clearly show neutral He emission at $\lambda\lambda$ 4471, 6678, and 7065. Despite the low S/N of the spectra taken on 2018 January 19 (due to weather and bad seeing), $H\alpha$ is visible in the bottom right panel of Fig. 5. Table 3 lists the emission equivalent widths of $H\alpha$ and $H\beta$. The upper panel of Fig. 6 shows the mean of MDM spectrum of S3, which appears similar to the two XLO spectra. All the XLO, APO and MDM spectra have similar continuum flux and moderate Balmer emission lines, indicating KZ Gem was in a similar accretion state during the observations.

⁴ The Gaia DR2 gives $\alpha = 06^{\text{h}} 53^{\text{m}} 02.^{\text{s}} 457$, $\delta = +16^{\circ} 39' 58''.67$ for this star (Arenou et al. 2018).

2.3. Photometry

Our differential time-series photometry is from the 1 K FlareCam with $1''.3 \text{ pixel}^{-1}$ when binned 2×2 mounted on the APO 0.5m Astrophysical Research Consortium Small Aperture Telescope (ARCSAT), and Andor CCD cameras on the XLO 0.85m and MDM McGraw-Hill 1.3m telescopes. We obtained 14 light curves spanning almost three years. For the XLO and ARCSAT data, we used star C1 (Fig. 1) as the comparison star, while for the MDM data we used S4, which was well-resolved from the DN. The MDM 1.3m data from 2016 February 13, 14, and 15 were obtained with a GG420 filter⁵ (hereafter, GG420-band), and no filter was used in four XLO observations with the 0.85m and 2.16m telescopes. The XLO and ARCSAT data were obtained using the Point Source Function (PSF) in IRAF standard routines due to the contamination from the two nearby objects S2 and S4. Five light curves were also obtained with Johnson-Cousins V filters (hereafter, V-band) on the APO 0.5m and MDM 1.3m telescopes. The ARCSAT data taken on 2016 November 29 was the only light curve obtained in a sdss *g* filter.

3. RESULTS AND DISCUSSION

3.1. Period analysis

Since the K2 data are defocused and KZ Gem is located in a crowded field, the wide aperture shown in the K2 image plot of KZ Gem in the Mikulski Archive for Space Telescopes (MAST)⁶ (Vanderburg 2014; Vanderburg et al. 2015) indicates that the SFF corrected light curve of KZ Gem includes the flux from several nearby stars. Hence, the orbital period of 0.22242 d (~ 5.34 hr) derived by Dai et al. (2017) from the blended K2 data needed further verification.

We were able to measure cross-correlation velocities of the secondary star in 55 of our MDM 2.4m spectra. The APO spectra did not yield cross-correlation velocities. We excluded the NaD λ 5893 blended absorption feature from the correlation region due to possible confusion with nearby He I λ 5876 emission. To search for periods, we constructed least-squares sinusoidal fits on a sufficiently dense grid of trial frequencies over the range of typical CV periods. Only a single period, corresponding to a single choice of cycle count between the observing runs, gave an acceptable result. A sinusoidal fit to the velocities of the form

$$Vel(t) = \gamma + K \sin[2\pi(t - T_0)/P_{\text{orb}}] \quad (1)$$

yielded the parameters listed in Table 4. T_0 is the time when the secondary star passes from blue to red through the mean velocity (i.e., the inferior conjunction of the secondary star). The orbital period found in the search, and refined using Equation 1, is $P_{\text{orb}} = 0.2224628(2)$ d, near 5.34 hr, in good agreement with the period derived from the K2 photometry. The uncertainty is small because the cycle count is unambiguous over more than 4 years. To further verify this derived period, we carried out an absorption velocity periodogram shown in Fig. 7 using a ‘residual-gram’ method described by Thorstensen et al. (1996). A significant peak of this periodogram is at the frequency of 4.4951 d^{-1} coincident with P_{orb} . Although the APO spectra could not contribute to the absorption line fit, the 18 APO H α emission line velocities, obtained over a ~ 46 hr time base, corroborate the result, giving $P_{\text{orb}} = 0.225(3)$ d, consistent with the absorption-line result. Fixing the period of the emission-line

⁵ The GG420 filter blocks light at wavelengths $< 4200 \text{ \AA}$ and is approximately equivalent to no filter.

⁶ <https://archive.stsci.edu/prepds/k2sff/html/c00/ep202061320.html>

fit to that derived from the absorption lines produces a scatter ($\sigma \sim 44 \text{ km s}^{-1}$), which is larger than typically found. The best-fitting emission velocity curves shown in Fig. 8 display large deviations around phase 0.75 – 1.0, when a hotspot would have a maximum contribution. Hence, this may be caused by a hotspot. The ephemeris for the inferior conjunction of the normal star, T_{inf} , derived from the absorption line velocities is

$$T_{\text{inf}} = \text{BJD } 2457434.9280(7) + 0^{\text{d}}.2224628(2) E, \quad (2)$$

where E is the cycle number, and the time base is UTC.

Using this ephemeris, we phased and stacked the 2019 January and February MDM modspec data to create a phase-resolved greyscale image (lower panel of Fig. 6). Before averaging, we rectified the spectra and edited out cosmic rays and other artifacts. The many absorption features of the late-type secondary are seen Doppler-shifting back and forth with phase. The $\text{H}\alpha$ emission line moves in anti-phase to the absorption lines, consistent with an origin in the disk/hotspot surrounding a white dwarf. Assuming that the motion of the emission lines traces the motion of the white dwarf like a long-period DN TT Crt (Szkody et al. 1992), the mass ratio of the two component stars may be roughly estimated to be 0.81 using the relationship,

$$q = \frac{M_{\text{rd}}}{M_{\text{wd}}} \sim \frac{K_{\text{em}}}{K_{\text{abs}}}, \quad (3)$$

where K_{em} and K_{abs} correspond to the amplitudes of the best-fitting radial velocity curves derived from the emission and absorption lines. A range of $q = 0.74 - 0.88$ is derived by considering the 2σ errors of K_{em} and K_{abs} listed in Table 4, though larger systematic errors are possible.

3.2. Secondary Spectrum

We used the parameters in Table 4 to shift the MDM 2.4m spectra to the rest frame of the secondary as described in Section 2.1. The Green et al. (2018) 3-dimensional reddening maps show little extinction in this direction out to $\sim 2 \text{ kpc}$, so we did not apply any reddening correction to the spectrum before decomposing. The decomposition process yielded acceptable results for spectral types K0 through K5, and suggest that around half the light in the 5000-6500 Å region arises from the secondary star. Fig. 6 shows one of the most successful of the decomposition, for a K2V star HD109011, scaled to a flux equivalent to $V = 17.9$. The flux calibration is typically accurate to $\sim 0.2 \text{ mag}$, limited by cloud and losses at the $1''.1$ spectrograph slit.

3.3. Light-curve morphology

3.3.1. The variable orbital modulation

Compared with the high-precision orbital period derived from the velocities, a periodogram derived from our differential time-series photometry, based on the Lomb-Scargle periodogram method (Lomb 1976; Scargle 1982), shows a notable period of 0.484 d almost twice P_{orb} . Although a trivial peak at the period of 0.221 d can also be found in this periodogram, a large discrepancy of $\sim 2 \text{ min}$ from P_{orb} implies that the orbital modulation of KZ Gem is complex and noisy.

Fig. 9 shows the 14 light curves in four bands (GG420, sdss g , no-filter and V) spanning from 2016 to 2018, phased using the spectroscopic ephemeris (Equation 2). All show variable double-hump modulations with a full amplitude of $\sim 0.3 \text{ mag}$, which is compatible with a pure ellipsoidal

modulation (e.g., 0.2 – 0.3 mag [Bochkarov et al. \(1979\)](#); [McClintock et al. \(1983\)](#)). The consistent amplitude implies that the source was quiescent for all our observations. Our observations from different filters and different nights do, however, differ in detail. For brevity, we will refer to phases 0.0, 0.25, 0.5 and 0.75 as the secondary dip, the secondary hump, the primary dip, and the primary hump, respectively.

Table 5 lists minimum and maximum times and their corresponding phases, derived using parabolic fits to the light curves with uncertainties estimated by a bootstrap method. Although most phases are close to 0.0, 0.25, 0.5 or 0.75, the largest O-C of the primary hump, observed on 2018 November 07, is 26 min from its typical phase of 0.75. However, the following secondary hump just shows a small deviation of 6 min from phase 0.25. Due to the variations in the orbital modulation, the O-Cs of the light minima or maxima cannot be used to determine orbital period variations, as commonly used for many eclipsing DN (e.g., Z Cha ([Dai & Qian 2009](#)) and V2051 Oph ([Qian et al. 2015](#))).

The double-hump modulation is less distinct in the single sdss *g*-band light curve observed on 2016 November 29, due to the large scatter and relatively short duration of the observation. Fig. 10 shows the normalized and phased light curves in the other three bands superposed to demonstrate the variations in the orbital modulation in the different bands. The three sequential days of GG420-band light curves show more typical double-hump modulations with a higher-level primary hump (0.75) and lower-level primary dip (0.5), similar to other dwarf nova (e.g., J0632+2536 and TW Vir ([Dai et al. 2018](#))). However, the three no-filter-band light curves obtained 2017 December 25, 2018 November 01 and December 31 (panels c, d and h in Fig. 9) display two humps at the same flux level and much deeper (by ~ 0.1 mag) primary dips. This is more like a pure ellipsoidal modulation with equal maxima and the deepest minimum around phase 0.5 caused by the tidal distortion of the Roche-lobe-filling secondary star ([Bochkarov et al. 1979](#)). For KZ Gem, the amplitude of the V-band ellipsoidal variation is larger than that of the long-period DN TT Crt (<0.2 mag) derived by [Szkody et al. \(1992\)](#).

Panel d of Fig. 9 shows that the lower-level secondary hump (0.25) detected on 2018 March 08 can rise to the level of the primary hump in eight months. Compared with the no-filter-band ellipsoidal modulation on 2018 December 31 (panel h of Fig. 9), the light curve observed three days earlier (panel g of Fig. 9) with the same filter and telescope (XLO 2.16m) clearly shows the typical double-hump modulation. Although the three V-band light curves plotted in panel f of Fig. 9 display ellipsoidal modulation similar to the no-filter-band light curves, their individual descending branches around phases 0.25 – 0.5 show slight variations in the primary dip or secondary hump. The V-band light curve with a long duration of 6.22 hr taken on 2018 November 07 presents an atypical modulation in that the primary hump is lower than the secondary hump, similar to the long-period CV CXOGBS J174444.7260330 ([Ratti et al. 2013](#)). The normalized V-band light curves superposed in the bottom panel of Fig. 10 confirm this atypical double-hump modulation, which is opposite to the modulations in GG420 and no-filter bands (the upper two panels of Fig. 10). In summary, the orbital modulation of KZ Gem sometimes appears as a pure ellipsoidal modulation, and sometimes switches to a typical DN double-hump modulation.

3.3.2. *Transient Events*

Although transient events have been detected in many low-state magnetic CVs (e.g. [Kafka & Hoard 2009](#); [Araujo-Betancor et al. 2005](#)), similar reports for quiescent dwarf nova are rare. Inspection of Fig. 11 shows 5 transient events that have an almost symmetric profile (i.e., nearly equal rise and

fall) rather than an exponential profile as detected in typical X-ray/optical flares found in polars (e.g. Dai et al. 2013; Terada et al. 2010). Since two of the five events are dips rather than brightening events (humps), a simple parabolic function may be more appropriate to fit them than a Gaussian function. The details of the transient events as listed in Table 6 show that the observed symmetric events last longer and have smaller amplitudes than those detected in the low-state polar AM Her (Dai et al. 2013).

The g -band light curve shown in the top panel of Fig. 11 displays two sequential brightening events with the nearly equal timescale of ~ 30 min. The peak of the first one almost occurs at the light minimum of the primary dip, while the second has a smaller amplitude. This resembles the two R-band brightening events with similar amplitudes and durations that occurred at the beginning of the low-to-high state transition in the prototype polar AM Her (Dai et al. 2013). Since most of the brightening events (flares) detected in cool stars showing typical exponential profiles are detected in a red R band and have a range of amplitude $0.02 \sim 0.3$ mag (e.g. Qian et al. 2012; Zhang et al. 2010), the twin brightening events in the blue sdss g band may not originate from the secondary star of KZ Gem, but are likely related to the white dwarf or the inner part of the disk. The three brightening events of KZ Gem have shorter durations, smaller amplitudes, and more symmetric profiles than the quasi-periodic mini-outbursts detected in Kepler observations of two other DN (V1504 Cyg Osaki & Kato 2014, and CRTS J035905.9+175034 Littlefield et al. 2018), which had a duration of ~ 2 d, amplitudes of ~ 0.5 mag and irregular morphologies. This implies that the brightening events might have a different origin than the mini-outbursts of the other two DN. In the bottom panel of Fig. 11, a brightening event in the no-filter band occurring at phase 0.04 (close to the light minimum of the secondary dip), has the longest duration of 64 min and the smallest amplitude of 0.093 mag.

The two significant dips in the no-filter band with similar amplitude and duration observed on 2018 March 08 and November 01 are shown in the middle two panels of Fig. 11. The former appears at the peak of the primary hump (0.75), while the latter is slightly asymmetric and occurs ~ 20 min ahead of phase 0.75 (i.e., the egress branch of the V-shaped primary hump). In the no-filter-band light curve detected on 2018 December 31, a less distinct dip with a short duration (~ 9 min) and small amplitude (~ 0.05 mag) appears at phase 0.74. Thus, the detected brightening and dip events in KZ Gem at quiescence seem to be related to the secondary light minima and the primary light maxima, respectively.

3.4. Synthetic analysis

Dai et al. (2018) proposed a phenomenological model to reproduce the double-hump light curves of low-inclination DN, and successfully obtained photometric solutions for three DN by using the light curve code XRBinary developed by E. L. Robinson⁷ and the nonlinear fitting code NMfit. This demonstrated the reliability of the model obtained using the codes. We attempted to use this model to carry out a complete synthetic analysis for KZ Gem based on our followup ground-based light curves spanning ~ 3 years.

All 13 light curves with the GG420, no-filter, and V bands were separated into three types. Since the no-filter-band and V-band light curves consist of data observed by many different telescopes on several separated nights, they show larger scatter than those in the three-day sequential GG420-band light curves with a total of ~ 4000 data points. Due to the higher orbital phase resolution and

⁷ <http://www.as.utexas.edu/~elr/Robinson/XRbinary.pdf>

smaller scatter, we derived a light curve model for KZ Gem from the overlapped GG420-band light curve shown in the top panel of Fig. 10. Before running XRBinary, the light curve was first binned with a phase resolution of 0.01. Since the main feature of the orbital light curve is the variable ellipsoidal modulation, the two stellar component stars dominate the flux contributions to the light curve, like the DN TT Crt (Szkody et al. 1992) and J0632+2536 (Dai et al. 2018). At times, one or more hotspots on the disk may change the orbital modulation from a pure ellipsoidal modulation to a typical DN double-hump modulation. The amplitude of the $H\alpha$ emission line variation in the greyscale plot (bottom panel of Fig. 6) is evidence of an S-wave indicating the motion of a hotspot on the disk similar to the trailed spectra of the DN SDSS J0116+09 (see Fig. 3 of Szkody et al. 2018). Hence, two models, model-1 (no surface hotspot) and model-2 (a surface hotspot) were investigated.

3.4.1. System parameters for KZ Gem

Based on the data from RKcat and other literatures, the averaged white dwarf masses for three grades (A: well-measured; B: less-well-measured; C: without error bars) are $0.82 M_{\odot}$, $0.78 M_{\odot}$ and $0.74 M_{\odot}$, respectively. They are similar to the previous prediction of $0.83 \pm 0.23 M_{\odot}$ for CVs in average (Zorotovic et al. 2011). Because the white dwarf mass of KZ Gem is not accurately determined, we preset the initial M_{wd} to $0.83 M_{\odot}$ as a starting point of the iterations, rather than a fixed or assumed parameter. Since the derived orbital period of KZ Gem is above the period gap, an average CV white dwarf temperature of $\sim 25,793$ K derived by Sion (1999); Urban & Sion (2006) was assumed to be the initial T_{wd} . The NaD absorption line shown in the two XLO and mean MDM spectra (Fig. 4 and 6) implies a late K star in KZ Gem. The initial temperature and mass of the secondary star (T_{rd} and M_{rd}) was assumed to be 4410 K and $0.67 M_{\odot}$, respectively. Since a preparatory accretion disk model derived by fixing the masses and temperatures of the two component stars to be the initial parameters in the NMfit program implies the accretion disk almost extends to the surface of the white dwarf, R_{in} is always equal to R_{wd} during the iterations.

Based on the phased and binned light curve in GG420 band, all 17 (13 for model-1) parameters were set to be adjustable. With model-1, the best-fit light curve shows a large deviation from the observed light curve at phases 0.0 – 0.25. However, this deviation can be eliminated using model-2. A much smaller χ^2 indicates that model-2 with two default limits: $R_{\text{in}}=R_{\text{wd}}$ and $0.74 \leq q \leq 0.88$ gives a better fit than model-1. The best-fitting parameters and their uncertainties were estimated by the code NMfit. The modeled light curve in the GG420 band is plotted in the top left-hand panel of Fig. 12. For KZ Gem, the irradiation effect is not calculated by XRBinary as $L_{\text{rd}} > L_{\text{wd}} + L_{\text{d}}$. Although an accurate white dwarf mass cannot be obtained from our light curves due to the almost constant flux contributions from the white dwarf ($\sim 4\%$) to the system light, the appropriate physical parameters of the white dwarf can be roughly limited within a small range of q . A search using white-dwarf mass covering a range from 0.6 – $1.1 M_{\odot}$ indicates that the χ^2 only shows a small change from 14 to 17, and the minimal χ^2 is found at $0.86 M_{\odot}$ consistent with the average mass for CVs found from the detailed study by Zorotovic et al. (2011). Based on the MK spectral classes (Cox 2000), a normal K0V star is estimated from $T_{\text{rd}} = 5120(\pm 110)$ K. The derived $M_{\text{rd}} \sim 0.7(\pm 0.2) M_{\odot}$ indicates a later K type dwarf. Hence, our light curve model demonstrates that the secondary of KZ Gem is an early K-type dwarf in accord with the observed spectra. Like the other long period DN TW Vir and J0632+2536 (Dai et al. 2018), M_{rd} and R_{rd} of KZ Gem are basically consistent with the semi-empirical mass-radius relation of CV donor sequence (Knigge 2006; Knigge et al. 2011), and the CVs mass/radius-period relations (Warner 2003; Smith & Dhillon 1998) shown in the bottom left-hand and two right-hand panels

of Fig. 13, respectively. To verify the mass of the secondary star derived in this synthetic model, further high-resolution observations are needed. The top left-hand panel of Fig. 13 indicates that T_{rd} of KZ Gem is ~ 900 Kelvin higher than the prediction of the semi-empirical CV donor sequence (Knigge 2006; Knigge et al. 2011). This implies that the secondary star has undergone some nuclear evolution. The other three DN investigated by Dai et al. (2018) shown in the top left-hand panel of Fig. 13 may also have evolved donors similar to KZ Gem. Hence, these four DN appear to be Peculiar Cataclysmic Variables (PCVs) containing evolved donors (Rebassa-Mansergas et al. 2014; Ren et al. 2018).

3.4.2. Disk models in three bands

Five best-fitting system parameters (q , i , M_{wd} , T_{wd} and T_{rd}) derived from the GG420-band light curve were fixed to model the 12 parameters of the disk in three bands. The derived parameters listed in Table 7 are used to visualize a system configuration of KZ Gem using Phoebe 2.0⁸. All three 2D CV configurations at phase 0.75 shown in the middle panels of Fig. 12 indicate a consistent disk model consisting of a large, cool and thick disk with a flat temperature distribution around a central white dwarf with a mass of $0.86(\pm 0.09) M_{\odot}$, and two hotspots (one at the vertical side of the edge of the disk, which we will call hotspot^{es} and the other one on the surface of the disk (hotspot^{ss})). The luminosity of hotspot^{es} is given by $\dot{M}_{\text{rd}} \simeq L_{\text{acc}} R_{\text{out}} / GM_{\text{wd}}$. From this, we roughly estimate a range of mass transfer rate to be $2.7 - 7.9 \times 10^{-10} M_{\odot} \text{yr}^{-1}$ due to the different L_{acc} in different bands. This corresponds to a mass loss timescale (i.e., $\tau_{\dot{M}} \simeq M_{\text{rd}} / \dot{M}_{\text{rd}}$) in the range of $0.9 - 2.5 \times 10^9$ yr, far larger than the thermal (or Kelvin-Helmholtz) timescale of the secondary star ($\tau_{\text{kh}} \sim 9 \times 10^7$ yr). This is generally the case for CV secondaries (Patterson 1984). The secondary star is somewhat smaller in radius than an isolated main sequence star of the same mass, which may imply an overestimated \dot{M}_{rd} . Therefore, the mass transfer via the L1 point should be much slower and the secondary is always able to maintain thermal equilibrium.

The right-hand panel of Fig. 12 shows the relative flux contributions in percentage from the different model components calculated by XRBinary. The size of the disk in the three bands is similar, while the thickest disk appears in the V band. Note that the L_{d} in the no-filter band is only $\sim 30\%$ of that in the GG420 and V bands due to the cooler disk and smaller hotspot^{es} in the no-filter band. The zero points of the relative flux contributions from the different components listed in Table 8 indicate that two stellar components showing a pure ellipsoidal modulation dominate the system light in the no-filter band (i.e., the maximal percentage is close to 95%). Despite this, a weak hotspot^{es} at phase $0.72(\pm 0.03)$ distorts the pure ellipsoidal modulation into the typical double-hump modulation in the no-filter band. However, the averaged orbital modulation in the V band (with the relative flux contributions from the two component stars similar to that in the GG420 band), is an almost pure ellipsoidal modulation rather than the typical double-hump modulation. Investigation of the middle panels of Fig. 12 indicates that the hotspot^{es} in the GG420 band is larger than that in the V band, while the hotspot^{ss} in the V band with a similar size is located ahead of the one in the GG420 band. Moreover, the hotspot^{es} and hotspot^{ss} in the V band have roughly equal contributions to the primary and secondary humps. This may explain the nearly equal maxima of the two humps described by a pure ellipsoidal modulation. Hence, the geometric sizes, positions, and intensities of two hotspots may be the key parameters distorting the light curve from that of a pure ellipsoidal

⁸ The version of Phoebe used for the CV plotting is 2.0a2.

modulation. All three light curve models demonstrate that an ellipsoidal modulation caused by a K type dwarf dominates the orbital modulation of KZ Gem, and the variations in the two orbital humps result mainly from the two hotspots.

3.4.3. Comparison with the Gaia data

According to Equation (1) of Dai et al. (2018), a V-band magnitude of KZ Gem estimated from three parameters: the Gaia distance D_g , the system luminosity $L_{\text{all}} = L_{\text{rd}} + L_{\text{wd}} + L_{\text{d}}$ and a model-dependent bolometric correction BC_v , can be compared to the result obtained from the Gaia mission (Gaia et al. 2016).

The Gaia parallax of KZ Gem implies a distance $D_g = 1293 \pm 149$ pc (Luri et al. 2018). Since BC_v listed in three tabulations (Flower 1996; Bessell et al. 1998; Casagrande & VandenBerg 2014) are almost the same due to $T_{\text{rd}} > 4000$ K, we set BC_v to $-0.22(\pm 0.03)$, interpolated from the updated BC_v table proposed by Casagrande & VandenBerg (2014). The three disk models in different bands show different L_{d} , but a small range of $16.70 - 16.87$ mag for KZ Gem can be estimated from $L_{\text{all}} = 1.11 - 1.29 \times 10^{33} \text{ erg s}^{-1}$ due to the domination of $L_{\text{rd}} = 1.0 \times 10^{33} \text{ erg s}^{-1}$ ($> 75\%$ of the system light). Although the apparent visual magnitude of KZ Gem (S3) is not listed in SIMBAD, the estimated V-band magnitude is close to $B = 16.8$ mag listed in RKCcat, $sdss\ g = 16.74$ mag and $sdss\ r = 16.43$ mag listed in SDSS. Thus, the derived synthetic model of KZ Gem is compatible with the Gaia distance.

Like the two DN J0632+2536 and TW Vir (Dai et al. 2018), the T_{eff} of KZ Gem shown in the Gaia catalog is higher than the derived $T_{\text{rd}} = 5120(\pm 110)$ K listed in Table 7. This further confirms the previous speculation by Dai et al. (2018) that a higher T_{eff} derived by Gaia is common for DN due to possible contributions from hotter components in these systems (e.g., the white dwarf and disk). Note that the Gaia temperatures are determined from three broad bandpasses (Andrae et al. 2018) and the DR2 release notes urge caution in using them⁹.

4. CONCLUSIONS

Cross-checking several CV databases revealed a coordinate discrepancy of $9''$ for the DN KZ Gem. We obtained spectra of four nearby targets which show that the correct identification is a star matching the coordinates listed by RKCcat and VSX.

We used absorption-line radial velocities collected from 2014 to 2019 to improve the orbital period to $0.2224628(2)$ d. We collected light curves that show a variable double-hump modulation with a typical amplitude of ~ 0.3 mag. This orbital modulation shows night-to-night variations. We also detected three brightening and two dipping transient events with nearly symmetric rises and declines appearing around the orbital minima and maxima. The phased light curves are consistent with the high-precision spectral ephemeris.

The binned and normalized light curve in the GG420 band was analyzed using the light curve code XRBinary and nonlinear fitting code NMfit. The best-fitting synthetic model indicates that KZ Gem is composed of a primary white dwarf ($0.86(\pm 0.16) M_{\odot}$) and a Roche-lobe-filling K type dwarf ($0.7(\pm 0.2) M_{\odot}$) with an higher effective temperature ($5120(\pm 110)$ K) than the typical CV secondaries at the same orbital period (Knigge 2006; Knigge et al. 2011), orbiting each other with an orbital inclination of $51^{\circ}.6(\pm 1^{\circ}.4)$. The hotter secondary star implies that KZ Gem may be a new candidate of PCVs. By fixing the system parameters, a consistent disk model with a large, cool and

⁹ https://gea.esac.esa.int/archive/documentation/GDR2/pdf/GaiaDR2_documentation_1.0.pdf

thick disk with a flat temperature distribution including two hotspots near phase 0.75 was achieved for three bands of light curves. We estimate \dot{M}_{rd} to be $2.7\text{--}7.9 \times 10^{-10} M_{\odot} \text{yr}^{-1}$. All derived light curve models are in accord with results calculated from Gaia DR2 and indicate that a pure ellipsoidal modulation caused by a K type dwarf dominates the orbital modulation.

This work was partly supported by CAS Light of West China Program, the Chinese Natural Science Foundation (Nos. 11133007 and 11325315), and the Science Foundation of Yunnan Province (No. 2016FB007). PS acknowledges support from NSF grant AST-1514737. We acknowledge the support of the staff of the Xinglong 2.16m and 0.85m telescopes. This work was partially supported by the Open Project Program of the Key Laboratory of Optical Astronomy, National Astronomical Observatories, Chinese Academy of Sciences. Based on observations obtained with Apache Point Observatory 3.5m and the 0.5m Astrophysical Research Consortium Small Aperture Telescope, and the 1.3m and 2.4m at the MDM Observatory, operated by Dartmouth College, Columbia University, Ohio State University, Ohio University, and the University of Michigan. We thank Wang Huijuan (王汇娟) and Ren Juanjuan (任娟娟), for their great assistance on obtaining and reducing two XLO spectra taken on 2018 January 09 and 10.

Software: IRAF (Tody 1986, 1993), XRBinary (v2.4; Dai et al. 2018), NMfit (v2.0; Dai et al. 2018), Phoebe (v2.0; Prša et al. 2016))

REFERENCES

- Alam, S., Albareti, F. D., Allende Prieto, C., et al. 2015, *ApJS*, 219, 12
- Andrae, R., Fouesneau, M., Creevey, O., Ordenovic, C., & Mary, N. 2018, *A&A*, 616, 8
- Araujo-Betancor, S., Gänsicke, B. T., Long, K. S., et al. 2005, *ApJ*, 622, 589
- Arenou, F., Luri, X., Babusiaux, C., et al. 2018, *A&A*, 616, 17
- Armstrong, D. J., Kirk, J., Lam, K. W. F., McCormac, J., Walker, S. R., et al. 2015, *A&A*, 579, 19
- Armstrong, D. J., Kirk, J., Lam, K. W. F., McCormac, J., Osborn, H. P., et al. 2016, *MNRAS*, 456, 2260
- Bessell, M. S., Castelli, F., & Plez, B. 1998, *A&A*, 333, 231
- Bochkarov, N. G., Karitskaya, E. A., & Shakura, N. I. 1979, *Soviet Ast.*, 23, 8
- Boeshaar, P. C. 1976, Ph.D. Thesis
- Casagrande, L., & VandenBerg, D. A. 2014, *MNRAS*, 444, 392
- Cox, A. N. 2000, *Allen's Astrophysical Quantities* (AIP Press(Springer-Verlag))
- Dai, Z. B., & Qian, S. B. 2009, *ApJ*, 703, 109
- Dai, Z. B., Qian, S. B., & Li, L. J. 2013, *ApJ*, 774, 153
- Dai, Z.-B., Szkody, P., Garnavich, P. M., & Kennedy, M. R. 2016, *AJ*, 152, 5
- Dai, Z.-B., Szkody, P., Taani, A., Garnavich, P. M., & Kennedy, M. R. 2017, *A&A*, 606, 45
- Dai, Z.-B., Szkody, P., Kennedy, M. R., Su, J., Medagangoda, N. I., et al. 2018, *AJ*, 156, 153
- Downes, R. A., & Shara, M. M. 1993, *PASP*, 105, 127
- Downes, R. A., Webbink, R. F., & Shara, M. M. 1997, *PASP*, 109, 345
- Downes, R. A., Shara, M. M., Ritter, H., Kolb, U., et al. 2001, *PASP*, 113, 764
- Flower, P. J. 1996, *ApJ*, 469, 355
- Gaia Collaboration, Brown, A. G. A., Vallenari, A., Prusti, T., de Bruijne, J. H. J., et al. 2016, *A&A*, 595, 2
- Green, G. M., Schlafly, E. F., Finkbeiner, D., et al. 2018, *MNRAS*, 478, 651
- Hoffmeister, C. 1966, *AN*, 289, 139
- Kafka, S., & Hoard, D. W. 2009, *PASP*, 121, 1352
- Keenan, P. C., & McNeil, R. C. 1989, *ApJS*, 71, 245
- Knigge, C. 2006, *MNRAS*, 373, 484

- Knigge, C., Baraffe, I., & Patterson, J. 2011, *ApJS*, 194, 28
- Kukarkin, B. V., Kholopov, P. N., Efremov Y. N., Kurochkin N. E., Frolov M. S., et al. 1968, *IBVS*, 311, 1
- Kurtz, M. J., & Mink, D. J. 1998, *PASP*, 110, 934
- Lange, T. 2016, *BAVSR*, 65, 45
- Littlefield, C., Garnavich, P., Kennedy, M., Szkody, P., & Dai, Z. 2018, *AJ*, 155, 232
- Lomb, N. 1976, *Ap&SS*, 39, 447
- Luri, X., Brown, A. G. A., Sarro, L. M., Arenou, F., Bailer-Jones, C. A. L., et al. 2018, *arXiv*: 1804.09376
- McClintock, J. E., Petro, L. D., Remillard, R. A., & Ricker, G. R. 1983, *ApJL*, 266, L27
- Osaki, Y., & Kato, T. 2014, *PASJ*, 66, 15
- Patterson, J. 1984, *ApJS*, 54, 443
- Prša, A., Conroy, K. E., Horvat, M., Pablo, H., Kochoska, A., et al. 2016, *ApJS*, 227, 29
- Qian, S.-B., Zhang, J., Zhu, L.-Y., et al. 2012, *MNRAS*, 423, 3646
- Qian, S.-B., Han, Z.-T., Fernández, L., et al. 2015, *ApJS*, 221, 17
- Ratti, E. M., van Grunsven, T. F. J., Jonker, P. G., Britt, C. T., Hynes, R. I., et al. 2013, *MNRAS*, 428, 3543
- Rebassa-Mansergas, A., Parsons, S. G., & Copperwheat, C. M., et al. 2014, *ApJ*, 790, 28
- Ren, J., Rebassa-Mansergas, A., & Liu, X. 2018, *Proceedings of the 2nd International Conference on Big Data Research*, 196
- Ritter, H., & Kolb, U. 2003, *A&A*, 404, 301
- Scargle, J. D. 1982, *ApJ*, 263, 835
- Sion, E. M. 1999, *PASP*, 111, 532
- Smith, D. A., & Dhillon, V. S. 1998, *MNRAS*, 301, 767
- Szkody, P., Williams, R. E., Margon, B., Howell, S. B., & Mateo, M. 1982, *ApJ*, 387, 357
- Szkody, P., Everett, M. E., Dai, Z.-B., Serna-Grey, D. 2018, *AJ*, 155, 28
- Terada, Y., Ishida, M., & Bamba, A., et al. 2010, *ApJ*, 721, 1908
- Thorstensen, J. R., Patterson, J. O., Shambrook, A., et al. 1996, *PASP*, 108, 73
- Tody, D. 1986, *Society of Photo-Optical Instrumentation Engineers*, 627, 733
- Tody, D. 1993, *ASPC*, 52, 173
- Tonry, J., & Davis, M. 1979, *AJ*, 84, 1511
- Urban, J. A., & Sion, E. M. 2006, *ApJ*, 642, 1029
- Vanderburg, A. & Johnson, J. A. 2014, *PASP*, 126, 948
- Vanderburg, A. 2014, *arXiv*, 1412, 1827
- Vanderburg, A., Montet, B. T., Johnson, J. A., et al. 2015, *ApJ*, 800, 59
- Warner, B. 2003, *Cataclysmic Variables* (Cambridge: Cambridge Univ. Press)
- Zhang, L.-Y., Zhang, X.-L., & Zhu Z.-Z. 2010, *NewA*, 15, 362
- Zorotovic, M., Schreiber, M. R., & Gänsicke, B. T. 2011, *A&A*, 536, A42

Table 1. Coordinates and magnitudes of the 6 stars nearby KZ Gem listed in SDSS DR12^a

Name	R. A.	decl.	<i>u</i>	<i>g</i>	<i>r</i>	<i>i</i>	<i>z</i>
S1 ^b	06:53:02.74	+16:39:49.87	19.94(4)	18.67(1)	18.15(1)	17.96(1)	17.90(2)
S2	06:53:02.70	+16:39:53.98	21.66(12)	18.96(1)	17.56(1)	16.93(1)	16.60(1)
S3 ^c	06:53:02.45	+16:39:58.60	17.54(1)	16.74(-)	16.43(-)	16.30(1)	16.27(1)
S4	06:53:02.50	+16:40:05.99	16.22(1)	14.95(-)	14.59(-)	14.48(-)	14.49(-)
S5	06:53:01.81	+16:39:57.45	20.74(6)	19.38(1)	18.80(1)	18.55(1)	18.53(3)
S6	06:53:03.24	+16:39:56.15	21.50(10)	19.32(1)	18.23(1)	17.84(1)	17.66(2)

^a Alam et al. (2015).

^b Coordinates specified by the SDSS and SIMBAD.

^c Coordinates listed in RKcat and VSX.

Table 2. Summary of observations

UT Date	Observations	Filters/Spectrographs ^a	Exposures
2014 Dec. 14	MDM 2.4m	modspec	$2 \times 600s$ spectra
2016 Feb. 13-15	MDM 1.3m	GG420	$930 \times 10s$ images
2016 Nov. 29	APO 0.5m	sdss <i>g</i>	$415 \times 30s$ images
2016 Jan. 14-20	MDM 2.4m	modspec	$25 \times 600s$ spectra
2016 Feb. 11-15	MDM 2.4m	modspec	$5 \times 600s$ spectra
2016 Dec. 05 ^b	APO 3.5m	DIS	$1 \times 600s$ spectrum
2017 Jan. 22 ^c	XLO 2.16m	BFOSC	$1 \times 3600s$ spectrum
2017 Dec. 25	XLO 0.85m	no-filter	$149 \times 120s$ images
2018 Jan. 09	XLO 2.16m	BFOSC	$1 \times 2400s$ spectrum
2018 Jan. 10	XLO 2.16m	BFOSC	$1 \times 3600s$ spectrum
2018 Jan. 15 ^b	APO 3.5m	DIS	$2 \times 900s$ spectra
2018 Jan. 17	APO 3.5m	DIS	$6 \times 600s$ spectra
2018 Jan. 19	APO 3.5m	DIS	$3 \times 600s + 9 \times 900s$ spectra
2018 Mar. 08	XLO 0.85m	no-filter	$502 \times 30s$ images
2018 Nov. 01	XLO 0.85m	no-filter	$148 \times 90s$ images
2018 Nov. 05	APO 0.5m	V	$101 \times 150s$ images
2018 Nov. 07	APO 0.5m	V	$137 \times 150s$ images
2018 Nov. 14-20	MDM 2.4m	modspec	$6 \times 1200s$ spectra
2018 Nov. 15-17	MDM 1.3m	V	$420 \times 30s$ images
2018 Dec. 13-15	MDM 2.4m	OSMOS	$10 \times 1200s$ spectra
2018 Dec. 28	XLO 2.16m	no-filter	$165 \times 120s$ images
2018 Dec. 31	XLO 2.16m	no-filter	$201 \times 90s$ images
2019 Jan. 14	MDM 2.4m	OSMOS	$3 \times 900s$ spectra
2019 Jan. 16	MDM 2.4m	OSMOS	$4 \times 600s$ spectra

^aTwo spectra simultaneously taken by the DIS with the blue and red channels covering two wavelength ranges of 3900-5040 Å and 6225-7400 Å, respectively. The wavelength ranges of spectra taken by the OSMOS and BFOSC are 4200-7500 Å and 4600-8400 Å, respectively. A GG420 filter blocks light at wavelengths less than 4200 Å.

^bSpectra for S1.

^cSimultaneous spectra for S1, S2 and S4.

Table 3. S3 emission line equivalent widths

UT Date	H α (\AA)	H β (\AA)
2018 Jan 09	7.63(1)	—
2018 Jan 10	6.28(2)	—
2018 Jan 17	8.53(1)	1.67(1)
	8.89(1)	3.13(1)
	10.47(2)	3.52(1)
	10.21(2)	2.78(1)
	10.77(1)	3.90(1)
	8.68(2)	3.06(1)
2018 Jan19	7.52(4)	—
	5.17(2)	—
	5.23(3)	—
	5.62(8)	—
	5.18(8)	—
	4.53(1)	—
	6.49(2)	—
	7.31(3)	—
	6.20(4)	—
	5.44(7)	—
	6.49(3)	—
	5.26(3)	—

Table 4. Parameters of the sine fits for the radial velocities of KZ Gem

	γ km s $^{-1}$	K km s $^{-1}$	T_0 BJD (2450000+)	rms km s $^{-1}$
Absorption lines ^a	−13(±3)	191(±5)	7434.9280(7)	14
H α emission lines ^b	−15.7(±1.6)	154(±3)	8137.683(5)	44

^a 55 MDM spectra spanning from 2014 December to 2019 January.

^b 18 APO spectra taken on 2018 January 17 and 19.

Table 5. Light minimum and maximum times of KZ Gem

UT Date	BJD	Phase	hump/dip ^a	O-C
	2450000+			min
2016 Feb. 13	7431.8233(4)	0.044(4)	Sec.d	14
	7431.8700(3)	0.254(3)	Sec.h	1
2016 Feb. 15	7433.6524(3)	0.266(3)	Sec.h	5
	7433.7648(2)	0.771(3)	Pri.h	7
	7433.8253(2)	0.043(3)	Sec.d	14
2016 Nov. 29	7722.905(1)	0.495(6)	Pri.d	-2
2017 Dec. 25	8103.2044(9)	0.992(5)	Sec.d	-3
	8103.2591(5)	0.238(4)	Sec.h	-4
	8103.328(1)	0.547(6)	Pri.d	15
2018 Mar. 08	8186.0150(4)	0.236(4)	Sec.h	-4
	8186.0834(8)	0.544(5)	Pri.d	14
	8186.135(2)	0.78(1)	Pri.h	10
2018 Nov. 01	8424.3405(8)	0.541(5)	Pri.d	13
2018 Nov. 05	8428.899(2)	0.03(1)	Sec.d	10
	8429.005(4)	0.51(2)	Pri.d	3
2018 Nov. 07	8430.856(3)	0.83(1)	Pri.h	26
	8430.954(1)	0.270(6)	Sec.h	6
2018 Nov. 15	8438.9545(3)	0.233(3)	Sec.h	-5
	8439.0259(7)	0.554(4)	Pri.d	17
2018 Nov. 16	8439.9119(3)	0.537(3)	Pri.d	12
	8439.9683(4)	0.790(4)	Pri.h	13
2018 Dec. 28	8481.281(1)	0.496(5)	Pri.d	-1
2018 Dec. 31	8484.177(2)	0.51(1)	Pri.d	3
	8484.2352(4)	0.776(4)	Pri.h	8
	8484.291(1)	0.027(6)	Sec.d	9
	8484.3466(9)	0.277(5)	Sec.h	9

^aPri.h, Pri.d, Sec.h and Sec.d refer to the primary hump, primary dip, secondary hump and dip around phases 0.75, 0.5, 0.25 and 0.0, respectively.

Table 6. Transient excursions of KZ Gem

UT Date	Filter	BJD (Phase) ^a	Duration	Amplitude ^b
		2450000+		mag
2016 Nov. 29	sdss <i>g</i>	7722.904 (0.49)	28	+0.31
		7722.923 (0.58)	29	+0.26 ^c
2018 Mar. 08	no-filter	8186.018 (0.26)	44	-0.14
2018 Nov. 01	no-filter	8424.374 (0.69)	49	-0.16 ^c
2018 Dec. 31	no-filter	8484.295 (0.04)	64	+0.093

^a The times (phases) of the central peaks or dips of the transients.

^b The magnitude difference between the light maximum and minimum. The minus and plus before the digits denote that the transient is a dip and hump, respectively.

^c Calculated after removing slope changes.

Table 7. Photometric solutions for KZ Gem in three filters.

Parameter ^a	GG420	no-filter	V
q	0.81($\pm 0.2^b$)	–	–
i	51°. $6(\pm 1^\circ.4)$	–	–
White dwarf			
$M_{\text{wd}}(M_\odot)$	0.86(± 0.16)	–	–
$R_{\text{wd}}(R_\odot)$	0.0097 ^c	–	–
T_{wd}	16.9 ^d	–	–
L_{wd}	0.26 ^c	–	–
Red dwarf			
$M_{\text{rd}}(M_\odot)$	0.7 ^c (± 0.2)	–	–
$R_{\text{rd}}(R_\odot)$	0.65 ^c	–	–
T_{rd}	5.12(± 0.11)	–	–
L_{rd}	10.0 ^c	–	–
Accretion disk			
$R_{\text{in}}^e(R_\odot)$	0.0097	0.0097	0.0097
$R_{\text{out}}(R_\odot)$	0.647(± 0.004)	0.647(± 0.004)	0.61(± 0.03)
$H_{\text{edge}}(R_\odot)$	0.10(± 0.01)	0.238(± 0.035)	0.24(± 0.04)
ξ	–0.0045 ^d	–0.0027 ^d	–0.0095 ^d
L_{d0}	1.7(± 0.2)	0.36(± 0.18)	0.96(± 0.18)
L_{d}^c	2.6	0.8	2.3
Hotspot at the edge of the disk			
T_{es}	5.01(± 0.07)	4.50(± 0.22)	4.97(± 0.16)
ζ_{esmid} (phase)	0.821(± 0.007)	0.724(± 0.03)	0.85(± 0.02)
ζ_{eswidth} (phase)	0.21(± 0.02)	0.08(± 0.02)	0.09(± 0.02)
Hotspot on the surface of disk			
ζ_{ssmin} (phase)	0.73(± 0.05)	0.57 ^d	0.56(± 0.04)
ζ_{ssmax} (phase)	1.11(± 0.07)	0.94(± 0.16)	0.88(± 0.04)
$R_{\text{ssmin}}(R_\odot)$	0.52(± 0.01)	0.52(± 0.01)	0.52(± 0.01)
$R_{\text{ssmax}}(R_\odot)$	0.54(± 0.01)	0.54(± 0.01)	0.55(± 0.01)
$T_{\text{ratio}}^{\text{ss}}$	1.9(± 0.1)	2.3(± 0.4)	2.5(± 0.1)
χ^2	14.2	16.6	80.2

^a The unit of temperature and luminosity is 10^3 K and 10^{32} erg s^{–1}, respectively.

^b The uncertainty clearly larger than the preset range of q (0.74 \sim 0.88) was obtained after removing this limit during the iterations.

^c Calculated by XRBinary.

^d Insensitive to the observed light curves.

^e Fixed in NMfit program.

Table 8. Zero points of the relative flux contributions from different components

Components ^a	GG420	no-filter	V
Binary ^b	69.3	82.7	70.4
Disk ^c	9.6	0.01	3.5
Hotspot ^{es}	0.0	0.0	0.0
Hotspot ^{ss}	4.8	1.1	4.5

^a The relative flux contributions are in percentage.

^b Only consist of white dwarf and red dwarf.

^c Accretion disk without hotspot.

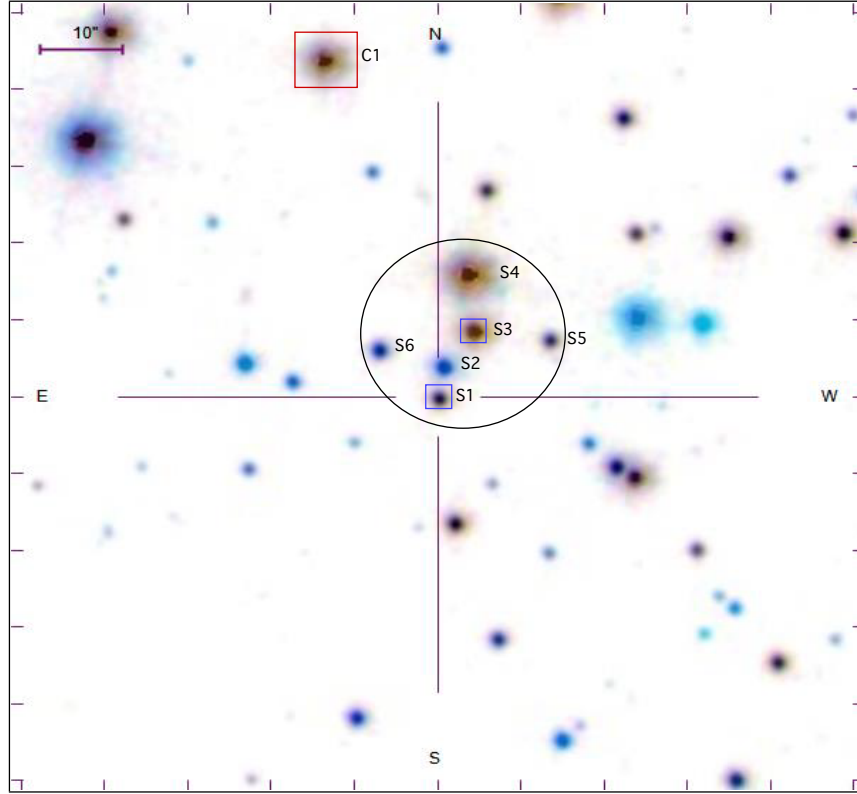


Figure 1. Finding chart of KZ Gem from the SDSS DR12 (Alam et al. 2015). The black circle is 15'' in radius. The star marked S1 corresponds to the coordinates in SDSS, SIMBAD, and K2, and S3 corresponds to the coordinates in RKcat, VSX, and Gaia. We show here that S3 is the dwarf nova. The comparison star C1 used for the XLO and APO photometry is marked with a red square; the MDM photometry used S1.

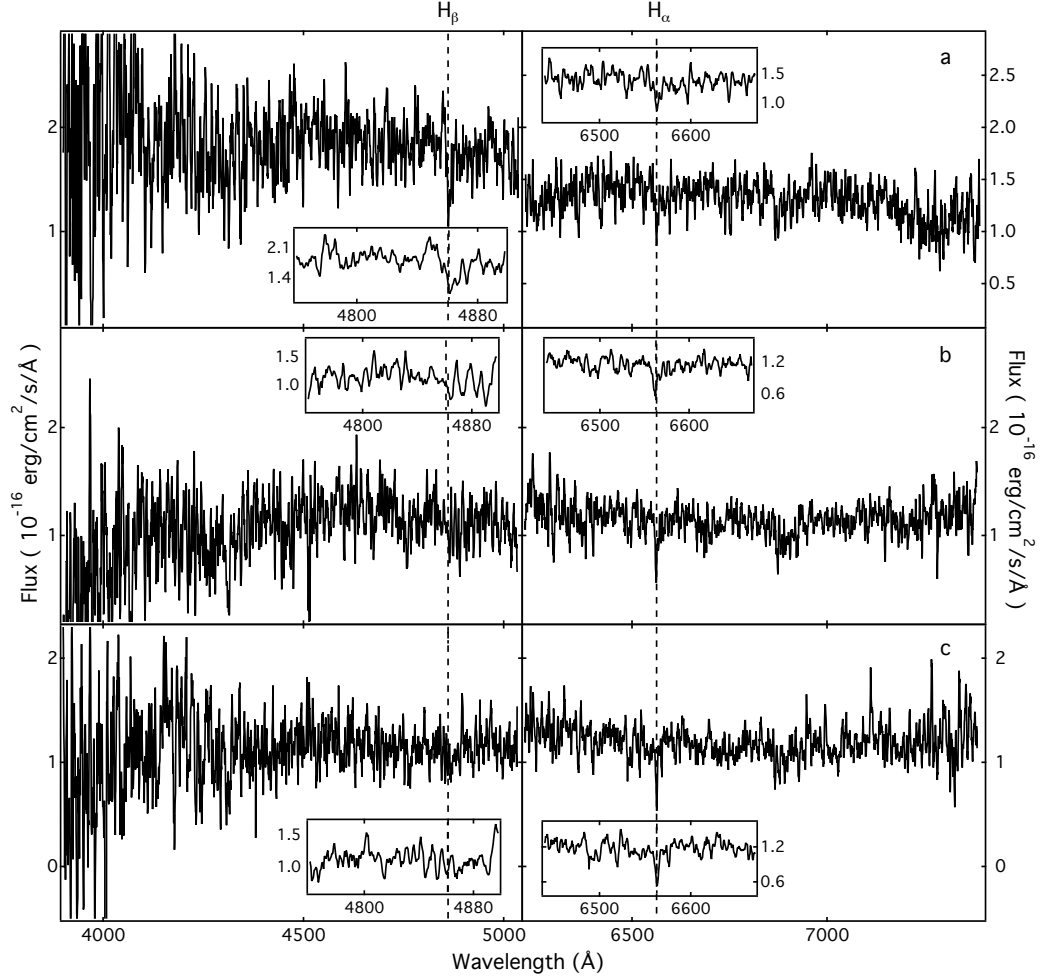


Figure 2. Blue and red spectra of S1 from the APO 3.5m telescope are shown in the left and right panels, respectively. From top to bottom, the spectra are from 2016 Dec. 05 (panel a) and 2018 Jan. 15 (panels b and c). The $H\alpha$ and $H\beta$ absorption lines are smoothed and marked by vertical dashed lines. The insets show the zoomed-in lines. $H\beta$ is not visible in the middle and bottom blue spectra.

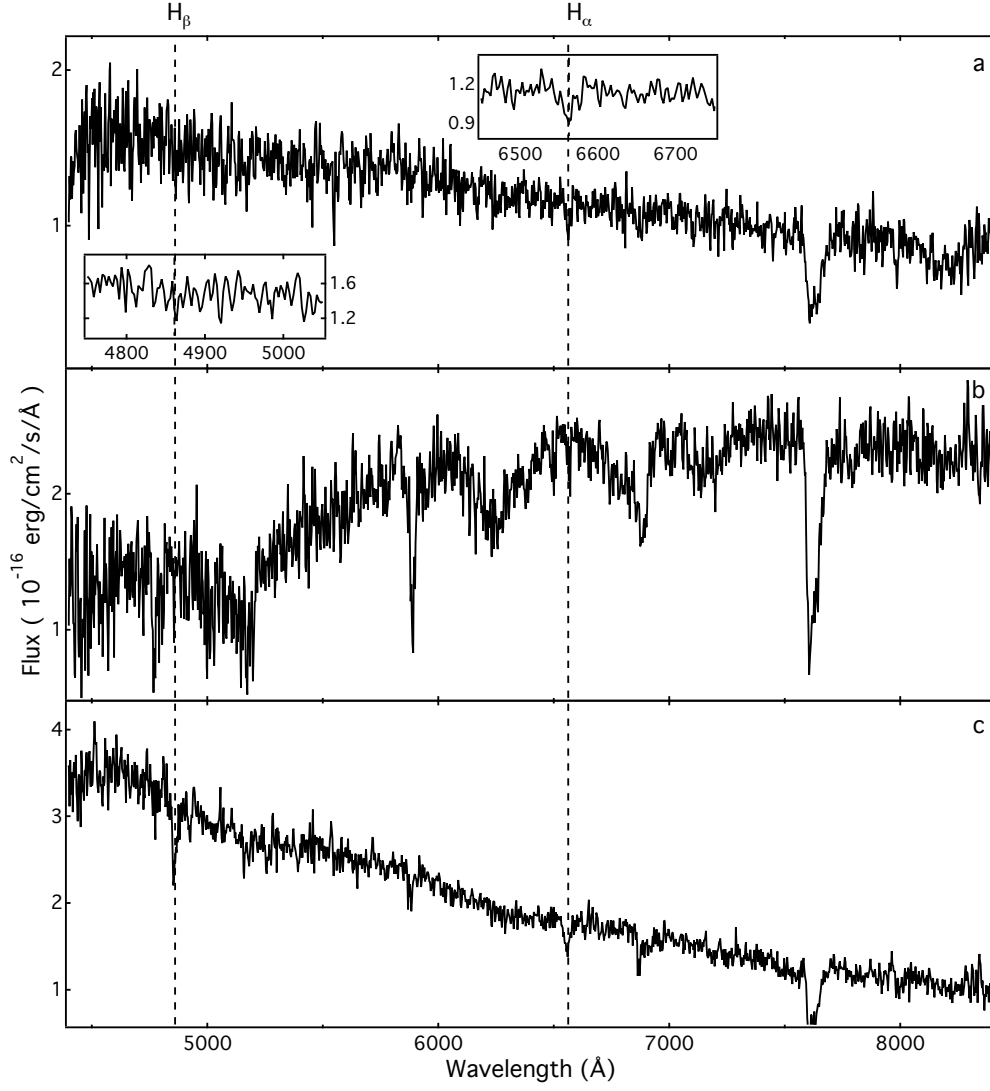


Figure 3. The spectra of S1, S2 and S4 located along the north-south direction were simultaneously taken by XLO 2.16m telescope on 2017 Jan. 22. In the top panel, the H α and H β absorption lines are smoothed and marked by vertical dashed lines. The zoomed-in lines are shown in the insets. The H β absorption line is not detected, as in the blue APO spectra shown in panels b and c of Fig. 2.

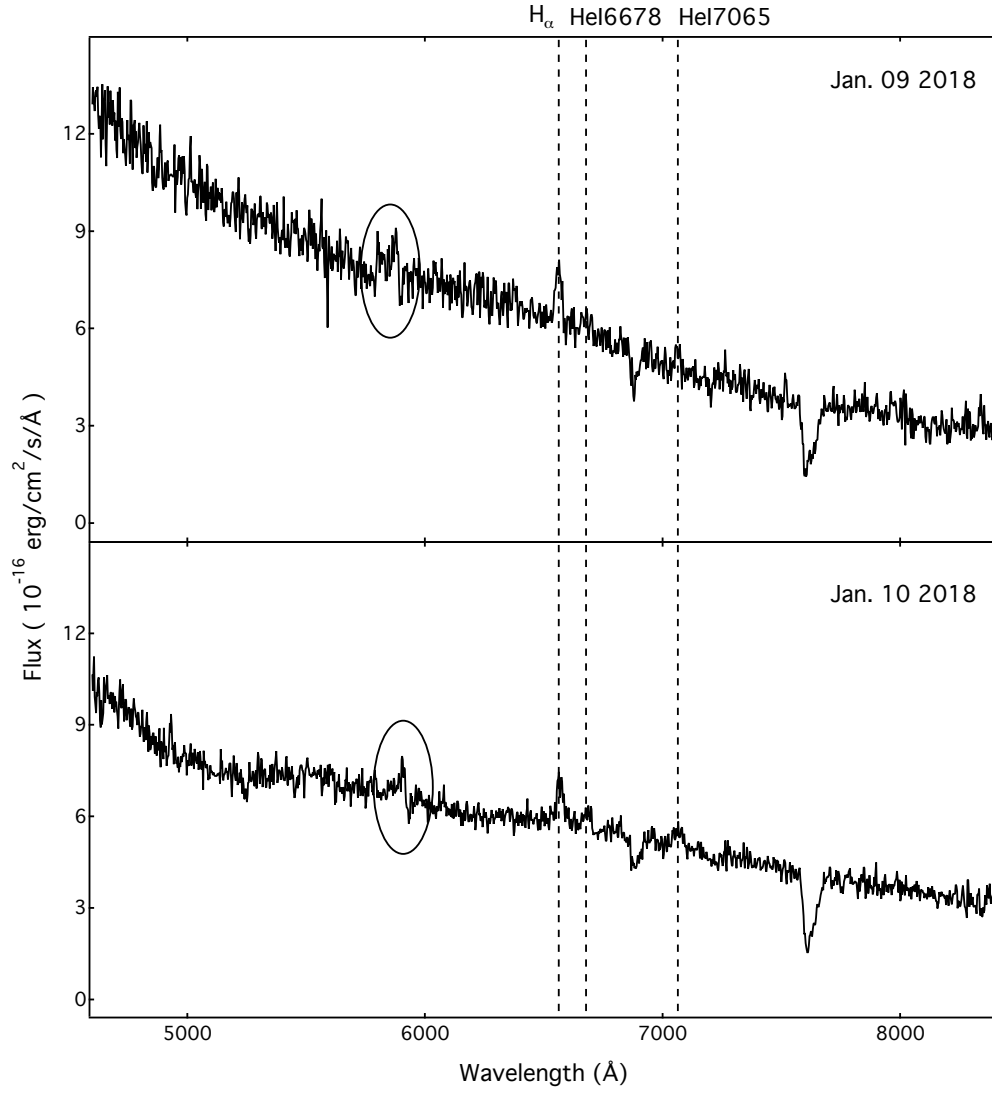


Figure 4. Two XLO spectra of S3 taken on 2018 Jan. 09 and 10 are shown in the upper and lower panels, respectively. The blended lines of the He I λ 5876 emission line and the weak absorption line NaD λ 5893 are marked by the black ovals.

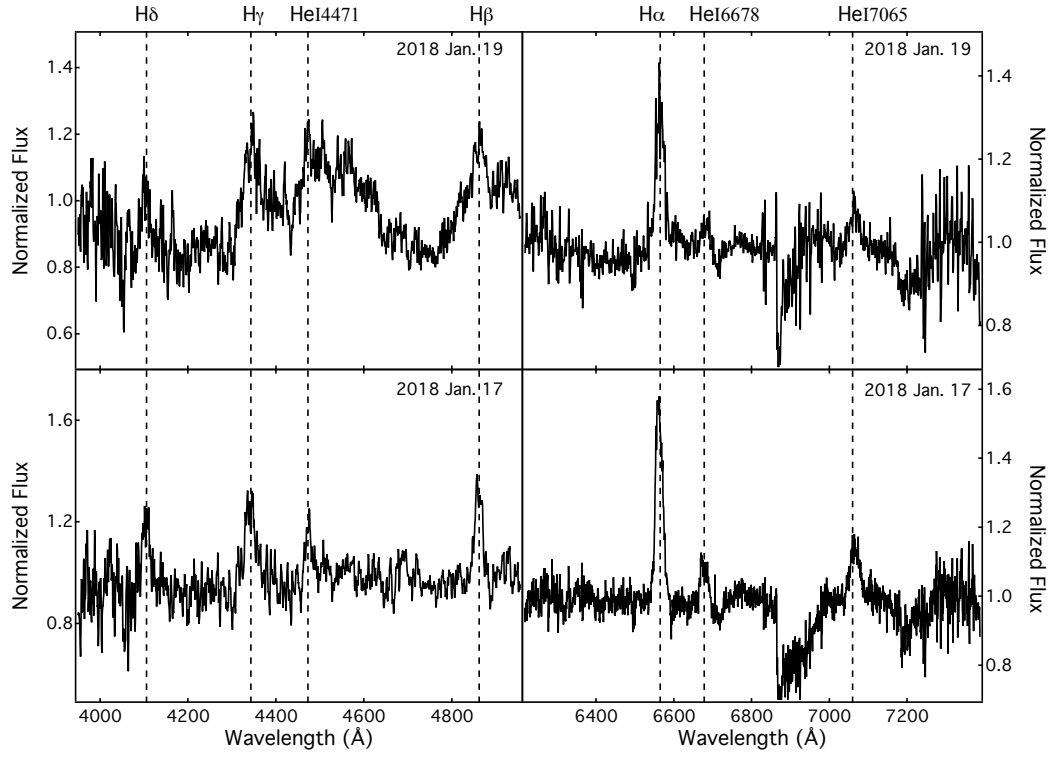


Figure 5. From top to bottom, mean APO spectra of S3 taken on 2018 Jan. 17 and 19 are shown. Blue and red spectra are plotted in the left and right panels, respectively.

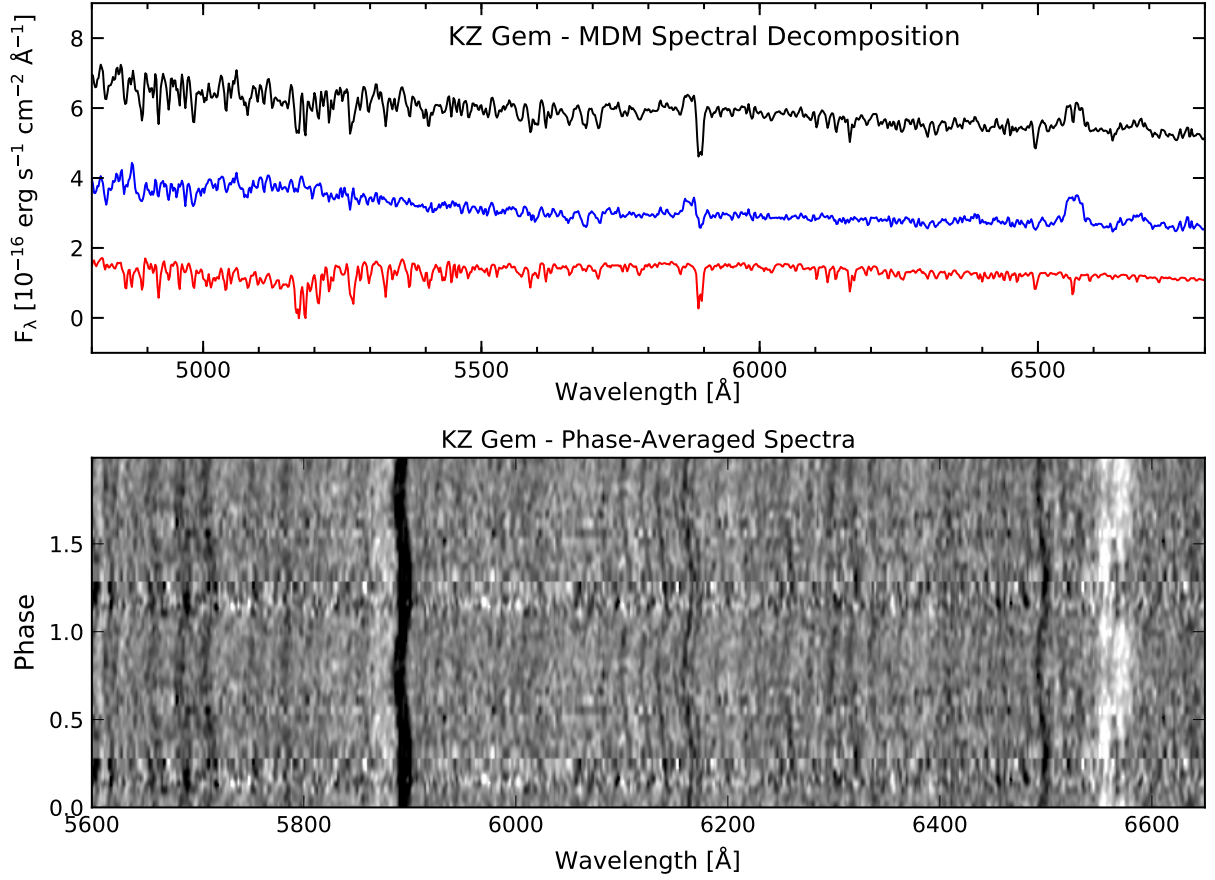


Figure 6. Upper panel: (Top trace; black) Mean MDM spectrum of KZ Gem in the rest frame of the secondary star. (Middle trace; blue) Mean spectrum after a scaled spectrum of a K2V star has been subtracted. (Lower trace; red) The scaled K2V star that was subtracted, shifted downward by 1.5 units to avoid overlap with the subtracted spectrum. Lower panel: rectified spectra from the MDM modspec arranged to form a phase-averaged greyscale image. Black and white colors are set to 0.8 and 1.2 times the continuum, respectively. The degrading signal-to-noise near phase 1.2, and a sharp discontinuity around phase 1.3 are artifacts of uneven phase coverage.

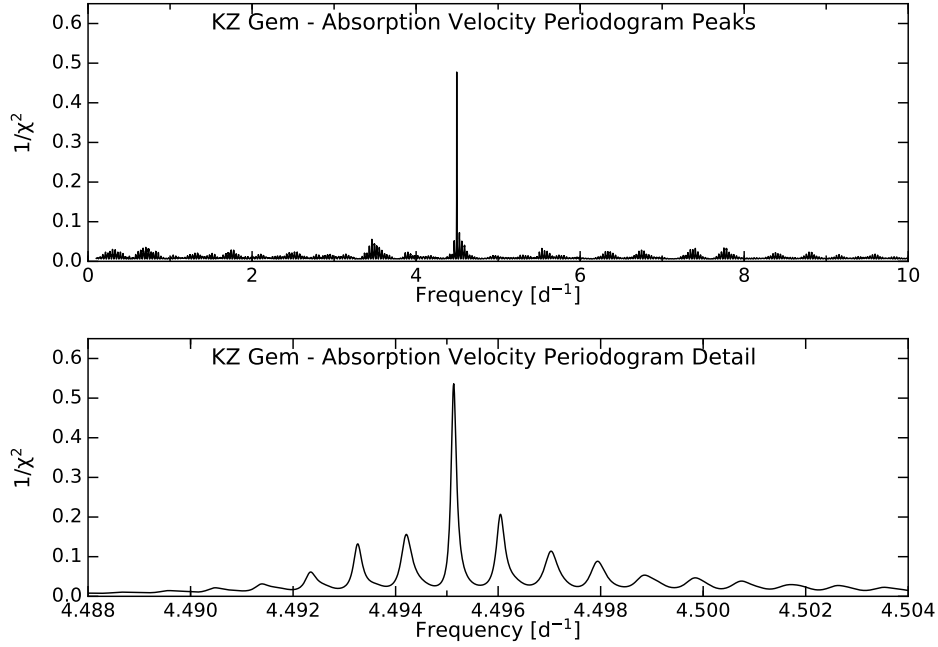


Figure 7. Periodogram of the absorption line velocities for KZ Gem. The top panel shows local maxima of the function joined by straight lines, to compress the plotting of the extremely fine grid of test frequencies necessitated by the ~ 3 -year span of the data. The lower panel shows the full periodogram, highly oversampled, in the neighborhood of the obvious peak. The flanking peaks correspond to frequencies differing by one cycle per ~ 1090 d.

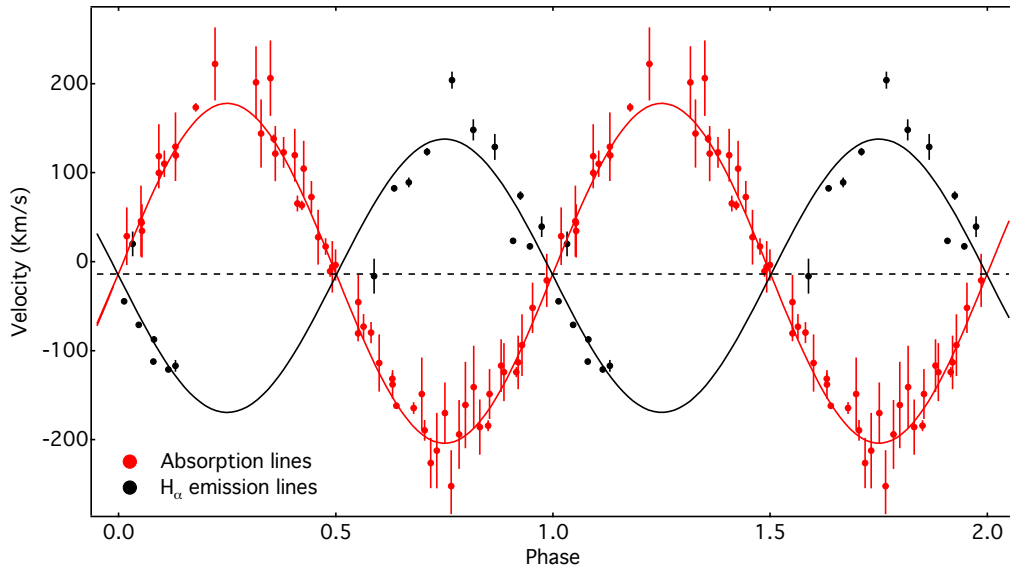


Figure 8. Radial velocities and best-fitting sinusoids folded using the ephemeris in Equation 1. The black circles and curve are from the APO emission ($H\alpha$) velocities, and the red are from MDM cross-correlation (absorption) velocities.

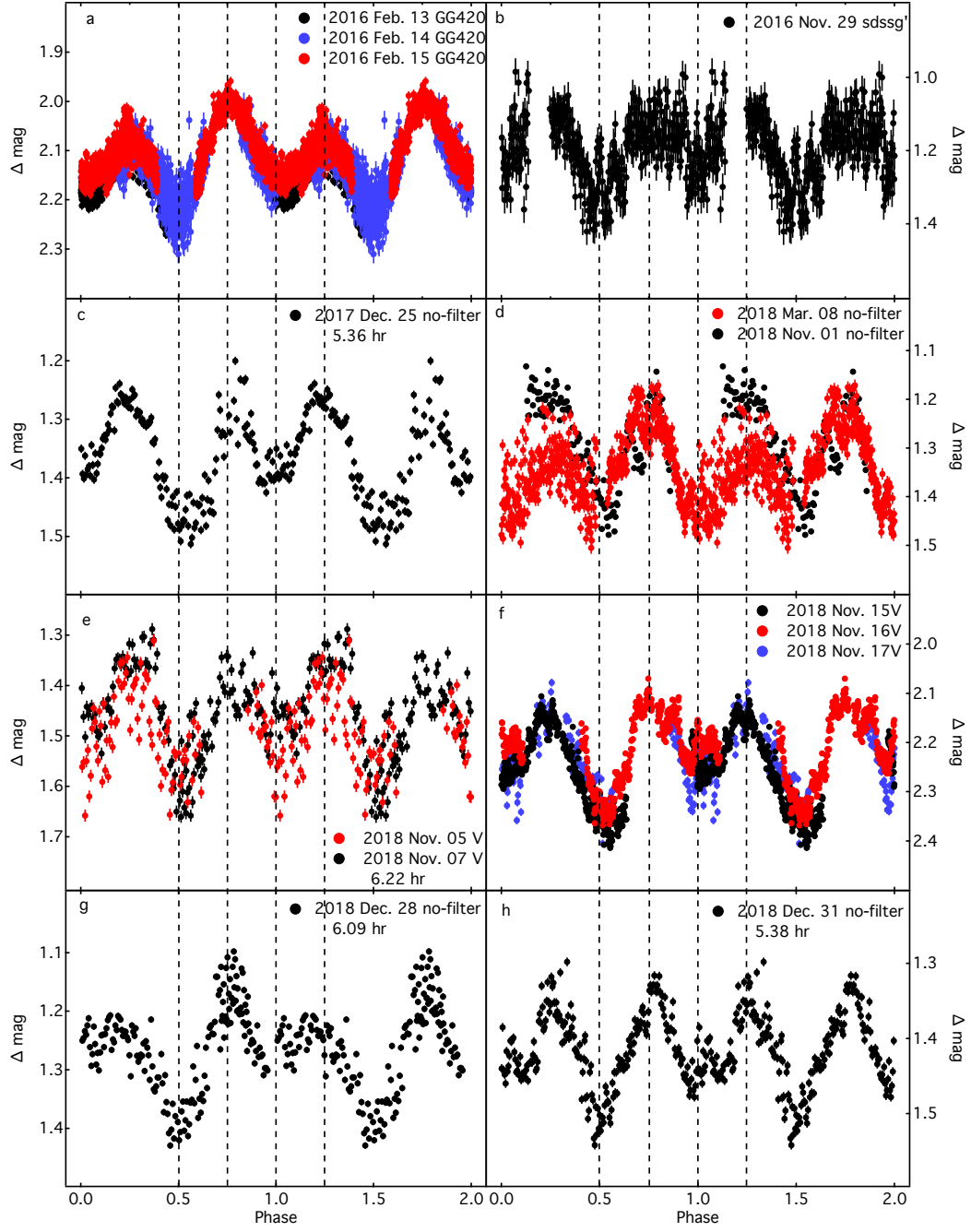


Figure 9. Fourteen differential light curves in sdss *g*, GG420, no-filter and V bands, phased with the ephemeris in Equation 2. The durations of light curves longer than the orbital period are listed with the legends. The error bars indicate the standard deviation (STD) of the magnitude difference between the comparison and check stars.

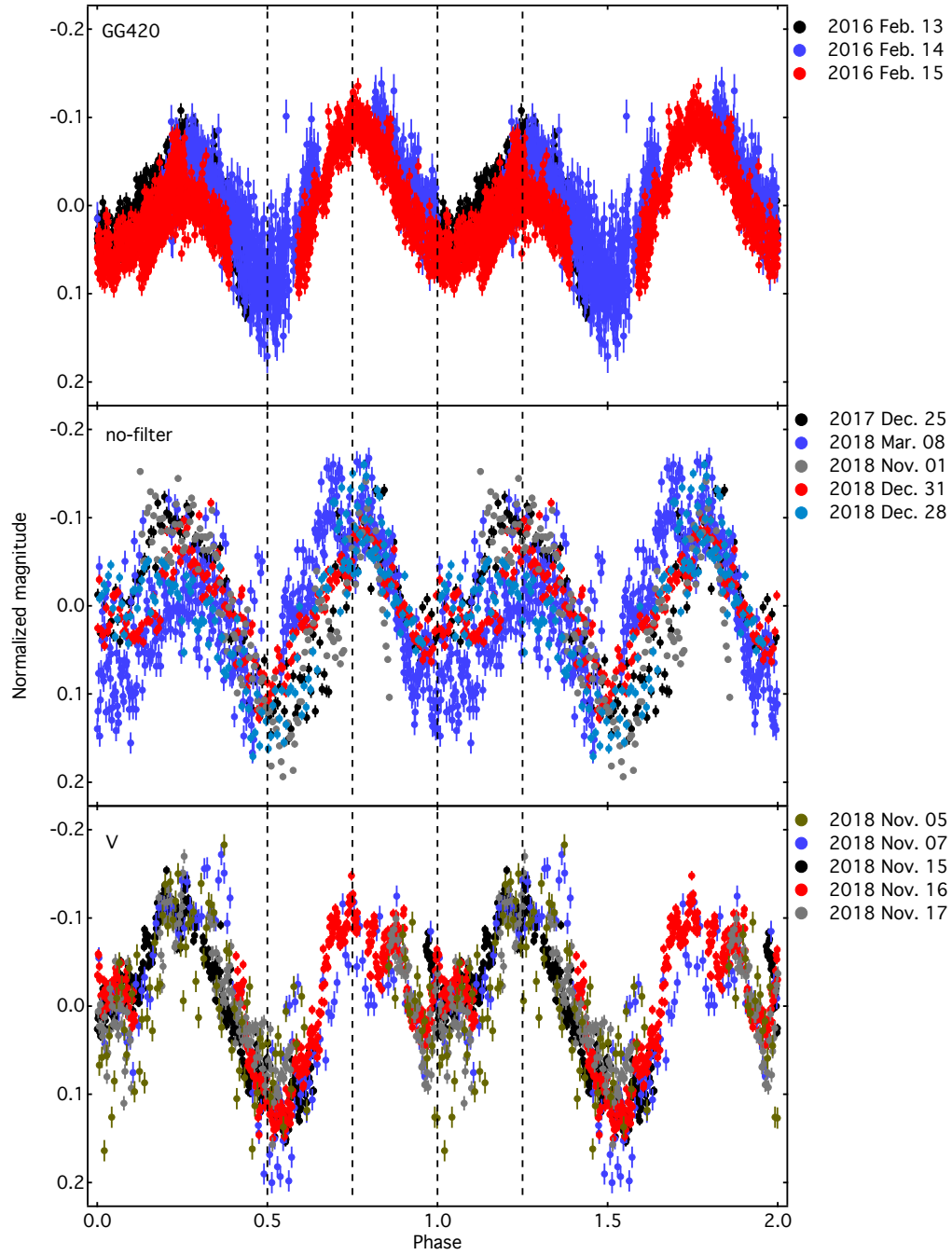


Figure 10. Thirteen normalized and phased light curves grouped into three bands: GG420, no-filter and V. The sdss g light curve obtained on 2016 November 29 is omitted. The different nights are distinguished by the colors listed in the legends.

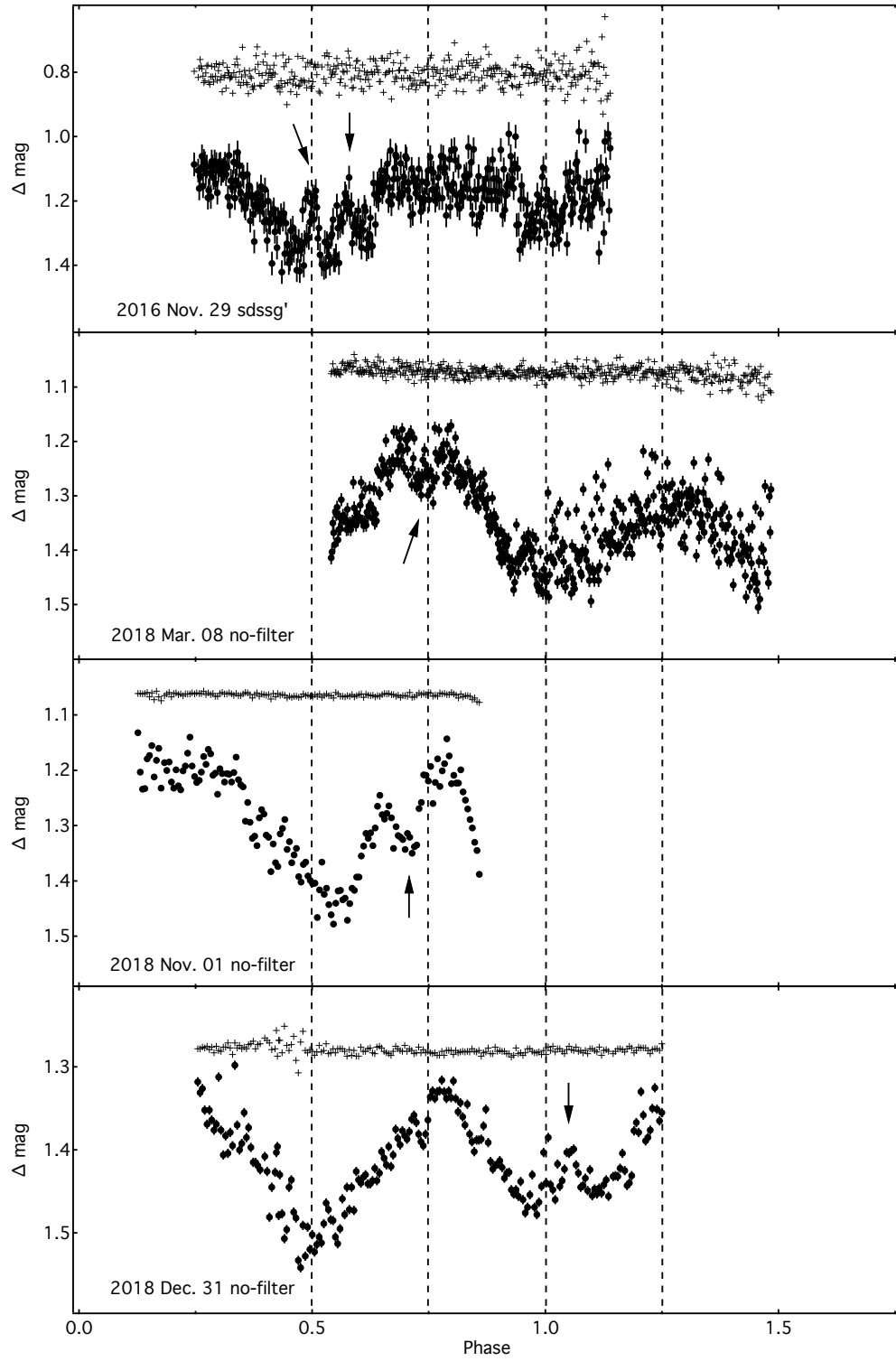


Figure 11. Four phased light curves showing five transient events (arrows) in time order from top to bottom.

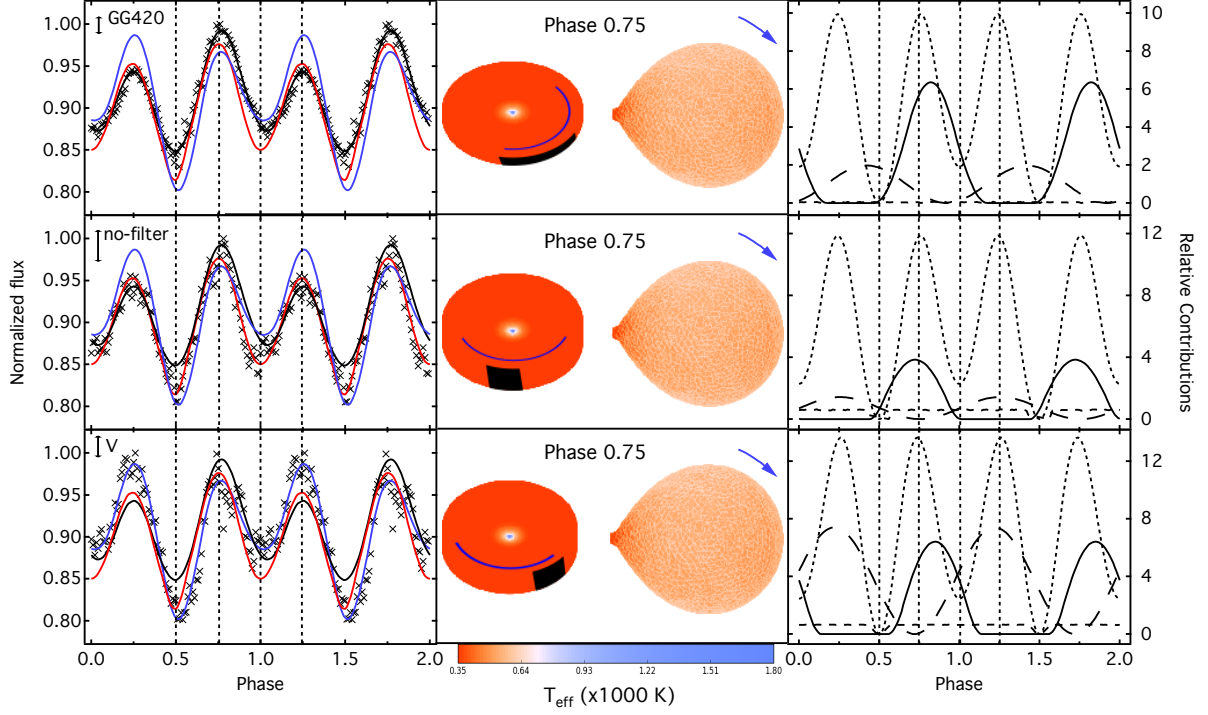


Figure 12. (Left panels): Phased, normalized and binned light curves in GG420, no-filter, and V, superimposed on the best-fitting light curves (black for GG420, red for no-filter and blue for V). The error bars in the top-left corners indicate the data scatter of the binned light curves. (Middle panels): The 2D binary configurations at phase 0.75 computed using Phoebe 2.0 from the fits to the different filters' data. The arrow shows the clockwise rotation of the binary. The colors in the 2D CV configuration denote the effective temperatures. The hotspot at the edge of the disk is filled in with black, rather than the color picked from the color bar, because the small temperature difference between the hotspot and the neighboring region of the disk reduces the contrast of the hotspot. (Right panels): Relative flux contributions from different components. The dotted and short dashed lines refer to the contributions from the two stellar components (white and red dwarfs) and the disk without the hotspots, respectively. The solid and long dashed lines denote the contributions from hotspot^{es} and hotspot^{ss}, respectively.

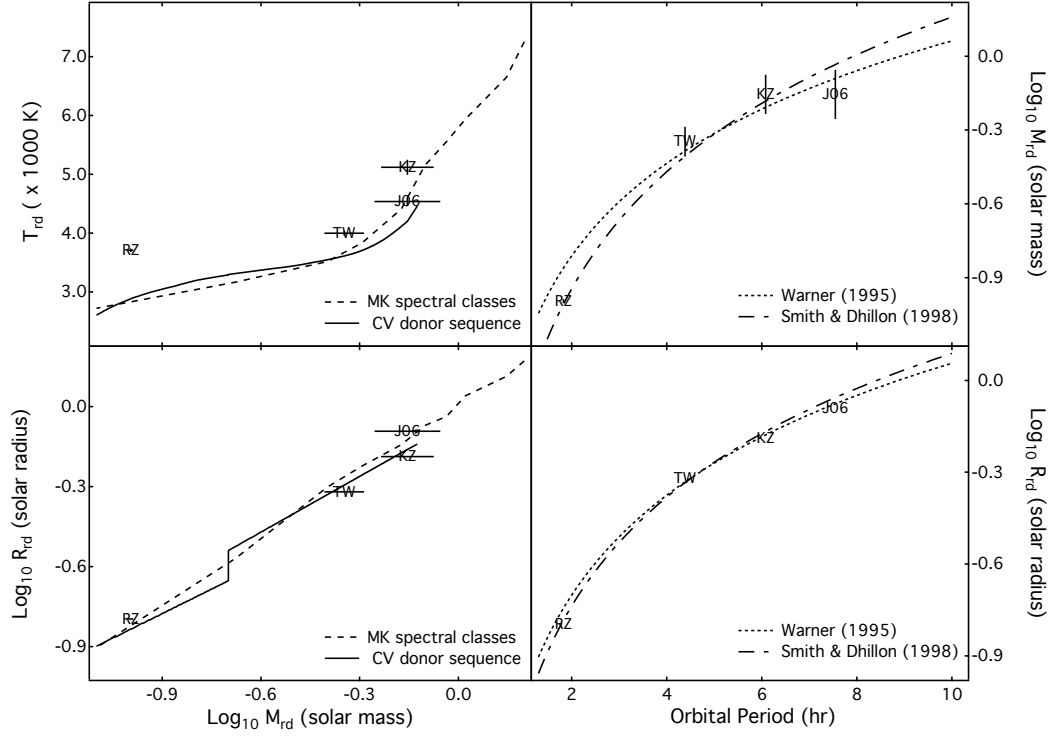


Figure 13. Four relationships of the secondaries. (Top left-hand panel): the relationship between the logarithm of mass and the effective temperature. (Bottom left-hand panel): the logarithm of mass-radius relationship. (Top right-hand panel): the period-mass relationship. (Bottom right-hand panel): the period-radius relationship. The dashed and solid lines denote the relationships based on the isolated low-mass stars (Cox 2000), and the semi-empirical CV donor sequence (Knigge 2006; Knigge et al. 2011), respectively. The dashed-dotted and dotted lines describe the relationships derived by Smith & Dhillon (1998) and Warner (2003), respectively. The data point marked by RZ, TW, J06, and KZ refer to the four DN: RZ Leo, TW Vir, J0632+2536 and KZ Gem, respectively.